MODELLING AND SIMULATION OF ASSEMBLY PROCESSES WITH ROBOTS

THOMAS MEITINGER*, F. PFEIFFER*

This paper deals with planning assembly processes for a manipulator using numerical simulations, so that the load on the parts and the dynamics of the robot during the part insertion can be studied. Typical for mating processes is the contact of the robot with its environment through the parts. The arising contact forces influence the motion of the robot. For numerical simulations we have to describe this operation by mechanical models. We present the dynamical model of the manipulator and models for mounting processes. Various methods are applied depending on the mechanical properties of the parts. With compliant mating parts, the forces and moments are only dependent on the relative position and the velocity of the robot's gripper with respect to the environment. If the mating parts are very stiff, the dynamics of the robot is characterized by closed loops, which requires special mathematical treatment. Numerical and experimental results illustrate our approaches.

1. Introduction

Small tolerances between the mating parts are often characteristic for mounting tasks. During the automatic assembly with a robot, the parts will contact each other due to uncertainties in the manipulator's position and in the parts' geometry. Undesirably high strains on the workpieces or even the unfeasibility of the task, e.g. due to jamming, may result. A well-known example for parts mating is the peg-in-hole problem. Many assembly processes can be reduced to this example. Thus the effects mentioned above can be studied.

There are three different approaches to handle these problems. One solution is the development of special passive compliant mechanisms, based on the Remote Centre of Compliance (RCC). Through this measure the area where no problems during the assembly might occur is enlarged. Such mechanisms were first developed for the peg-in-hole problem in two dimensions. In (Whitney, 1982) the analysis for designing the RCC was made quasistatically, whereas in (Asada and Kakumoto, 1988) the dynamics of the peg and the supporting mechanism were also taken into account. An extension to three dimensions can be found in (Strip, 1989). The same problem is considered in (Sturges, and Laowattana, 1994), where the principle of the Spatial Remote Centre of Compliance (SRCC) is used for the analysis.

---

* Lehrstuhl B für Mechanik, TU München, 80290 München, Germany,
  e-mail: tm@lbm.mw.tu-muenchen.de.

A second solution is the additional use of sensor information. Nearly all authors follow the same principle: First an initial contact state has to be identified. A new method for this step was introduced in (Farahat *et al.*, 1995). Various contact topologies in the presence of sensing and control uncertainties are tested. The method succeeds, even if the contact forces are statically indefinite. Then the peg has to be moved towards the hole. This phase can be called peg-on-hole (Bruyninckx *et al.*, 1995). Afterwards, the peg is aligned and inserted into the hole. Therefore, a two-point contact, which might lead to jamming, has to be avoided. For this phase in (Wapenhans *et al.*, 1992) an optimized controller is presented. If the operation fails due to sensing, model or control errors, the method of error detection and recovery is applied in order to complete the given task (Gottschlich and Kak, 1988; Jennings *et al.*, 1989; Steinle, 1996). In (McCarragher and Asada, 1992) all possible contact sequences are modelled as a discrete-event system using Petri nets. As new control methods appeared, they were also applied to the peg-in-hole problem, like fuzzy control (Park *et al.*, 1992) or neural networks (Park and Cho, 1995). In more recent investigations (Bergqvist *et al.*, 1994) additional sensors are utilized for not only detecting the contact state, but additionally finding out manufacturing defects like burrs and ruts.

The third approach is theoretical investigation. The insertion task is described by geometrical and mechanical models, where uncertainties from the robot's position, the robot's trajectory and the parts' geometry can also be taken into account. If the problem is solved by geometrical considerations and simple assumptions for the contact forces, one talks of fine motion planning (Lozano-Pérez *et al.*, 1984). In (Xiao and Zhang, 1995) an algorithm is presented which finds all possible contact points between polygonal-shaped objects in the presence of uncertainties. More insight into the peg-in-hole insertion is gained when additionally the stiffness of the supporting mechanism is considered and all contact forces are modelled. In (Whitney, 1982) for the two-dimensional case the area is calculated, where jamming and wedging might occur. In (Caine *et al.*, 1989) similar considerations are made for the same problem including three dimensions. The dynamics of the complete parts-mating process including a complete dynamic model of the manipulator is presented in (Seyfferth and Pfeiffer 1992). Every contact point is there closing a kinematical loop between the manipulator and the environment. For an efficient numerical implementation, the contact laws and transitions between the different contact states (no contact, sticking or sliding) are formulated as a Linear Complementarity Problem (LCP). The same method is applied to the three-dimensional peg-in-hole problem in (Meitinger and Pfeiffer, 1995a).

Different questions arise when regarding flexible workpieces. Through the compliance of the parts, effects like jamming and wedging are not likely to occur. In this case the forces and moments arising during the mating process are more interesting in order to evaluate the stresses and strains on the mating parts. For example, in (Meitinger and Pfeiffer, 1994) we have investigated the insertion of a piston with an elastic ring into a cylindrical hole. A widespread fixture in automated assembly are snap fasteners. In (Seyfferth and Pfeiffer, 1992) the unsteady force vs. distance graph is shown for the mating of a single snap joint under ideal conditions. A very detailed

three-dimensional model of snap-fasteners was presented in (Meitinger and Pfeiffer, 1995b), where a good correspondence between measurement and calculation of the forces arising during the mating process was achieved. An algorithm for the prediction of the motion of rigid parts interconnected by torsional springs was developed in (Donald and Pai, 1990). This theory was applied to the design of snap fasteners. In (Villarreal and Asada, 1991) more general considerations are made. A buffer zone is introduced to quantify the distributed compliance of the workpiece. The buffer zone indicates the permissible positional errors in a certain direction. However, the elasticity of the parts is modelled using as a simple force law: $F = Kx$. This theory is then applied to the assembly of a box with hinges and snap fasteners. The design of chamfers (the counterparts the compliant fixtures come in contact with) is investigated in (Whitney *et al.*, 1983). Various criteria, e.g. minimum insertion work, are used to calculate the shape of the chamfers. In this paper, we present the modelling of assembly processes which are executed by a manipulator. Thus we need on the one hand, a dynamical model of the robot which has to be coupled with the model of the parts-mating process.

In the next section, we will first introduce the dynamic model of the manipulator. An important section is the following one which concerns the determination of the contact points between the parts. Up to this point only the geometry plays a role. We will then describe both elastic and rigid parts. As examples for compliant work pieces we investigate snap joints and O-rings. When mating these parts together, the robot and the environment are nearly decoupled due to the compliance in the parts. Therefore quasistatic considerations are sufficient to describe the contact forces. Our examples for rigid parts are then a rectangular and a round peg put into the corresponding hole. If these bodies come into contact, the coupling with the environment is very stiff, so that we have additional constraints on the robot's dynamic. Depending on the number of contact points, the number of degrees of freedom in the system changes. The constraint equations between arbitrarily shaped parts are derived, as well as the contact laws and the conditions for the transition between different contact states. All our approaches are verified through a comparison of the calculated and measured forces acting on the robot's gripper during the insertion.

2. Robot Model

Before describing the models, we have to introduce the notation which we shall use in the following. Vectors are denoted by lower-case, bold-face characters (e.g. $a, b, \ldots$), matrices by upper-case bold-face characters (e.g. $A, B, \ldots$). Indices on the left refer to the coordinate system in which a vector is defined (e.g. $_Aa, {}_Ab, \ldots$).

The industrial robot, here a PUMA 560, possesses six axes and is modelled as a tree-like multibody system with rigid bodies and ideal links. As generalized coordinates we take the relative angles between the bodies

$$\gamma_A = (\gamma_{A1}, \gamma_{A2}, \gamma_{A3}, \gamma_{A4}, \gamma_{A5}, \gamma_{A6})^T \quad \in \mathbb{R}^6 \tag{1}$$

as shown in Fig. 1(a). Since the natural frequencies of oscillations due to the stiffness in the first three joints are in the range of interest, an elastic joint model is introduced.
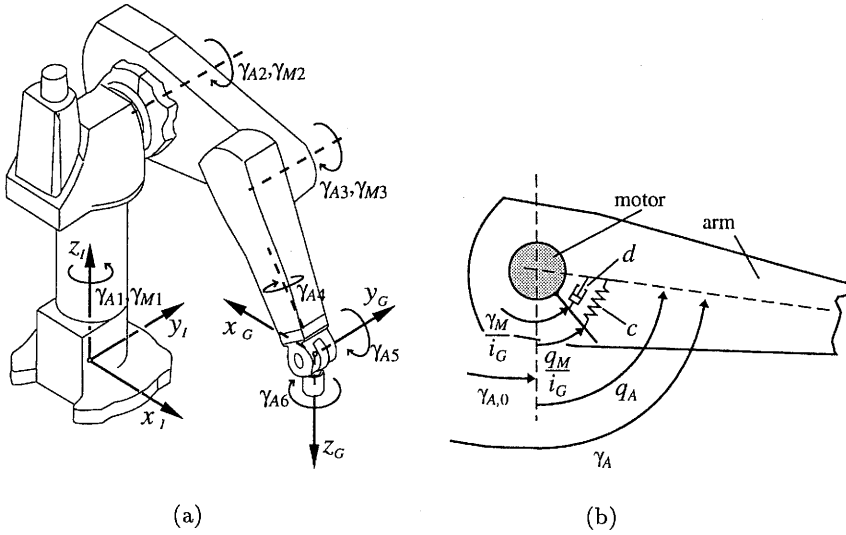
Fig. 1. The industrial robot PUMA 560 (a) and its joint model (b).

A link-joint unit consists of two bodies, the drive and the arm segment (Fig. 1(b)). They are coupled by a gear model

$$\tau_A = c\left(\frac{\gamma_M}{i_G} - \gamma_A\right) + d\left(\frac{\dot{\gamma}_M}{i_G} - \dot{\gamma}_A\right) \tag{2}$$

which is composed of the physical elements stiffness c and damping d. Thus three additional degrees of freedom are introduced between motor shafts and arm segments:

$$\gamma_M = (\gamma_{M1}, \gamma_{M2}, \gamma_{M3})^T \quad \in \mathbb{R}^3 \tag{3}$$

In the remaining links no joint model is necessary, because there the stiffness is high compared with the acting forces and the elasticity of these joints does not affect the system dynamics under consideration. Thus we have altogether nine degrees of freedom γ for our PUMA,

$$\gamma = (\gamma_M, \gamma_A)^T \quad \in \mathbb{R}^9 \tag{4}$$

The theory for derivation of the equations of motion for multibody systems like robots has existed for many years. As an example see (Johanni, 1987), where even elastic bodies are treated. For our PUMA we obtain a set of nine differential equations in the form

$$\overline{M}(\gamma)\ddot{\gamma} + \overline{h}(\gamma, \dot{\gamma}) = B\overline{u} \quad \in \mathbb{R}^9 \tag{5}$$

with the inertia matrix $\overline{M} \in \mathbb{R}^{9,9}$, centrifugal, Coriolois and gravitational forces summarized in the vector $\overline{h} \in \mathbb{R}^9$ and the control input $B\overline{u}$.

Since most mating tasks are limited to a small area of workpiece interaction, the robot motion will be slow and centrifugal and Coriolis forces in (5) may be neglected compared with gravitational and inertia forces. Hence the robot dynamics can be linearized around a working point γ_0, where $\dot{\gamma}_0 \equiv 0$. The vector

$$q = \gamma - \gamma_0 = (q_{M1}, q_{M2}, q_{M3}, q_1, q_2, q_3, q_4, q_5, q_6)^T \quad \in \mathbb{R}^9 \tag{6}$$

denotes the deviation from this working point. We obtain the following equations of motion:

$$M\ddot{q} + P\dot{q} + Qq = h + Bu \quad \in \mathbb{R}^9 \tag{7}$$

with the inertia matrix M, the damping matrix P and the stiffness matrix Q. The vector h contains the remaining gravitational forces. Bu regards the influence of the controller. For PD position control we have the typical form of the vector u:

$$u = -K_P \left(B^T q - q_D \right) - K_D \left(B^T \dot{q} - \dot{q}_D \right) \quad \in \mathbb{R}^6 \tag{8}$$

The matrices K_P and K_D contain the positional and velocity feedback gains. Through changing the desired positions and velocities q_D and $\dot{q}_D$ the motion of the manipulator along a trajectory is realized. Integrating the equations of motion (5) or (7), we obtain for every time step the position and orientation of the gripper (G-frame) with respect to the inertial fixed system (I-frame), as well as its translational and rotational velocity:

$$\underbrace{r_{IG}, \quad A_{IG},}_{\text{position and orientation}} \qquad \underbrace{v_G, \quad \Omega_G}_{\text{translational and angular velocity}} \tag{9}$$

which form the interface for the assembly process models.

3. Assembly Process with a Manipulator

Assembly tasks performed by a manipulator are characterized by the contact with the environment through the mating parts. Additional loads act on the robot's gripper and thus influence the motion of the manipulator. For numerical simulation, the dynamic model of the robot and the assembly process models have to be coupled.

Depending on the part's properties, there are two basic approaches to describe these loads. To illustrate this, we show in Figs. 2 and 3 a very simple example: a peg touching a flat surface with one point, where we shall demonstrate the basic ideas for both methods. If we deal with compliant workpieces, typically made of rubber or plastics, the coupling between the robot and the environment is weak. This is indicated in Fig. 2 on the left side through the small spring with stiffness c. In general, the forces f and moments m due to parts' deformation depend only on the position and the velocity of the gripper relative to the environment, i.e. the generalized coordinates q and their first time derivative $\dot{q}$:

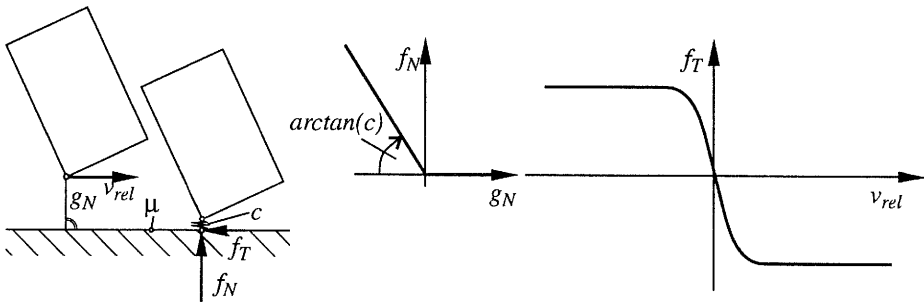$$f = f(q, \dot{q}), \qquad m = m(q, \dot{q}) \tag{10}$$

Fig. 2. Basic approach for compliant mating parts.

In the simple example of Fig. 2 we have only two contact forces f_N and f_T. The normal contact force depends on the relative displacement g_N in this direction in the case of contact $g_N < 0$ with a spring-like characteristic. In the tangential direction Coulomb's law is applied, however with a friction coefficient μ depending on the relative sliding velocity such that there is no jump at $v_{rel} = 0$. From this simple example the basic property of compliant mating parts can be recognized, namely there is always a functional relationship between the contact forces and kinematical values. The loads f and m are then imposed on the right-hand sides of the equations of motion (7):

$$M\ddot{q} + P\dot{q} + Qq = Bu + \left(J_T^T | J_R^T\right) \begin{pmatrix} f \\ m \end{pmatrix} \tag{11}$$

through a projection with the translational and rotational Jacobians J_T and J_R of the reference point at the gripper into the generalized coordinates of the system.

This basic approach is also possible for very stiff workpieces, e.g. made of aluminum or steel, but causes numerical problems. In our simple example, the stiffness c in the contact point becomes extremely high. With only small displacements very big reaction forces arise, which results in stiff differential equations. The contact forces have here a strong influence on the accelerations in the system $\ddot{q}$. Therefore another method is applied. The parts are regarded as rigid, which means also for our example in Fig. 3 that $c \to \infty$. Every contact point constrains the mobility of the robot. Two points coming into contact close a kinematical loop and thus reduce the number of degrees of freedom of the manipulator. The constraints g_i are unilateral:

$$g_i(q) \geq 0 \tag{12}$$

which means e.g. in the normal direction that the parts do not penetrate each other, if $g_i = g_N$ is the relative distance between two possible contact points. In the tangential direction unilateral constraints describe the unsteady character of friction and sliding. These two phenomena are also shown in Fig. 3 on the right. The equations

of motion (7) then additionally have to fulfil the constraint equations summarized in the vector g. This represents a system of differential-algebraic equations (DAE):

$$M\ddot{q} + P\dot{q} + Qq = Bu + W\lambda$$

$$g(q) \geq 0, \qquad \dot{g}(q,\dot{q}) \geq 0, \qquad \ddot{g}(q,\dot{q},\ddot{q}) \geq 0$$

(13)

where the vector λ contains the constraint forces. The matrix W is the constraint matrix which projects the constraint forces onto the degrees of freedom of the robot. The geometrical constraints g are needed on the acceleration level in order to combine them with the equations of motion, also describing accelerations.
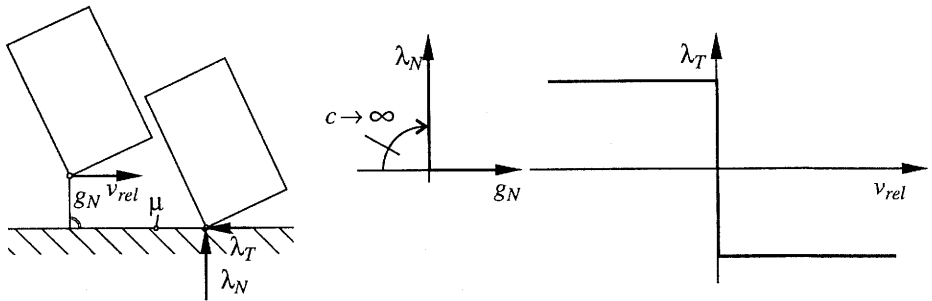
Fig. 3. Basic approach for stiff mating parts.

4. Contact Kinematics

In general the workpieces to be mounted are composed of surfaces Σ. Two patches of such mating parts which are not in contact yet are shown in Fig. 4. For their description we introduce additional frames. Fixed to the G-frame of the gripper, but with relative offset r_{GA} and relative orientation A_{GA}, the A-system is defined, in which the upper mating part is lying. Thus it is moving with translational and angular velocities v_G and Ω_G, respectively. The lower part is inertially fixed to the B-frame, which does not move, but has a relative distance and orientation to the inertial system of the robot r_{IB} and A_{IB}, respectively. All considerations will be made for the spatial case, which includes of course the planar description of the bodies in a plane. For the description of a surface we choose the vector form:

$$r_\Sigma(u,v) = \big(x(u,v), y(u,v), z(u,v)\big)^T$$

(14)

which is dependent on two parameters u and v. A curve for the planar case is only dependent on one parameter u. For example, a sphere (for the spatial case) and a circle (for the planar case) have the following parametrization:

$$\text{sphere: } r_\Sigma = \begin{pmatrix} R\cos v \cos u \\ R\cos v \sin u \\ R\sin v \end{pmatrix}, \quad \text{circle: } r_\Sigma = \begin{pmatrix} R\cos u \\ R\sin u \\ 0 \end{pmatrix}$$

(15)

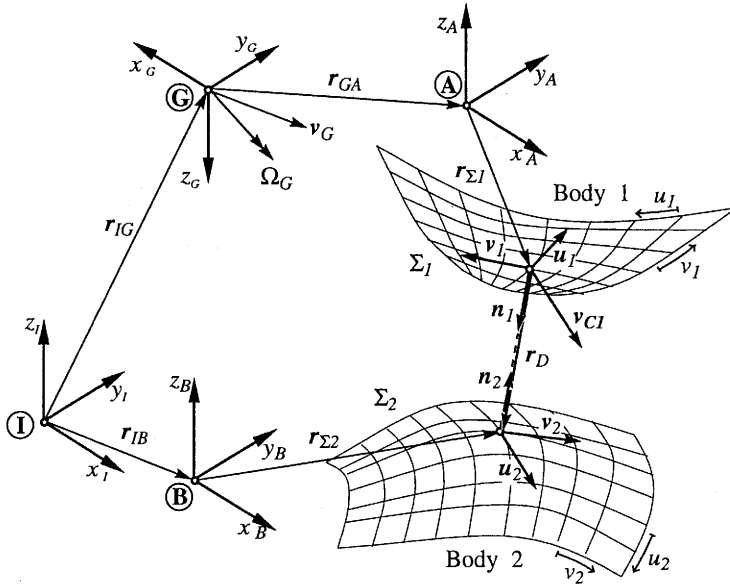Fig. 4. Two patches of a surface with one potential contact point.

where R stands for the radius. The values of $r_\Sigma(u,v)$, where $u_0 = $ const or $v_0 = $ const make a family of curves on the surface. Together they form a net of parameter lines, which can be also seen in Fig. 4. The partial derivatives of the vector r_Σ with respect to the parameters u and v are the tangent vectors u and v, respectively. They point along the parameter lines and span the tangent plane:

$$u(u,v) = \frac{\partial r_\Sigma}{\partial u}, \qquad v(u,v) = \frac{\partial r_\Sigma}{\partial v} \tag{16}$$

From these basic vectors the *fundamental magnitudes of the first order* are calculated:

$$E = u^T u, \qquad F = u^T v, \qquad G = v^T v \tag{17}$$

The normalized normal vector n is perpendicular to the tangent plane and points outwards the body:

$$n = \frac{u \times v}{\sqrt{EG - F^2}}. \tag{18}$$

We further need the *fundamental magnitudes of the second order*:

$$L = n^T \frac{\partial^2 r_\Sigma}{\partial u^2}, \qquad M = n^T \frac{\partial^2 r_\Sigma}{\partial u \partial v}, \qquad N = n^T \frac{\partial^2 r_\Sigma}{\partial v^2}. \tag{19}$$

For the determination of the contact points and later for the constraint equation we will need the partial derivatives of the normal $\partial n/\partial u$, $\partial n/\partial v$ and the tangents

$\partial u/\partial u$, $\partial u/\partial v$, $\partial v/\partial u$, $\partial v/\partial v$. With the formulae of *Weingarten* and *Gauss* this derivatives can be expressed in terms of the basic vectors:

$$\frac{\partial n}{\partial u} = \underbrace{\frac{FM - GL}{EG - F^2}}_{\alpha} u + \underbrace{\frac{FL - EM}{EG - F^2}}_{\beta} v, \quad \frac{\partial n}{\partial v} = \underbrace{\frac{FN - GM}{EG - F^2}}_{\alpha'} u + \underbrace{\frac{FM - EN}{EG - F^2}}_{\beta'} v \quad (20)$$

$$\frac{\partial u}{\partial u} = \Gamma_{11}^1 u + \Gamma_{11}^2 v + Ln, \qquad \frac{\partial u}{\partial v} = \Gamma_{12}^1 u + \Gamma_{12}^2 v + Mn \qquad (21)$$

$$\frac{\partial v}{\partial u} = \Gamma_{12}^1 u + \Gamma_{12}^2 v + Mn, \qquad \frac{\partial v}{\partial v} = \Gamma_{22}^1 u + \Gamma_{22}^2 v + Nn \qquad (22)$$

The definition of the *Christoffel symbols* $\Gamma_{\alpha\beta}^{\sigma}$, $\alpha, \beta, \sigma = 1, 2$, can be found e.g. in (Bronstein and Semendjajew, 1985).

In the following, we have to introduce additional indices because we regard two surfaces which might get in contact. The upper part held in the gripper of the manipulator is denoted by the index 1 $(\cdot)_1$, and the lower part connected to the environment by the index 2 $(\cdot)_2$. For a potential contact point we demand that the normal vector of body 1 (n_1) and the distance vector r_D be perpendicular to the tangent vectors of body 2 (u_2 and v_2). Then the two tangent planes on the surfaces are parallel and the contact points are lying just opposite each other, as shown in Fig. 4. Thus we obtain four non-linear equations:

$$f(x) = \left(n_1^T u_2 | n_1^T v_2 | r_D^T u_2 | r_D^T v_2\right)^T, \quad x = (u_1 | v_1 | u_2 | v_2)^T \qquad (23)$$

for four unknown parameters u_1, v_1, u_2, v_2 denoting the contact point. This non-linear problem has to be solved at every time step of the numerical integration. For better convergence of the root finder it is convenient to use the analytic derivates $\partial f(x)/\partial x$ which are defined through the partial derivatives (20)–(22) as

$$\frac{\partial f(x)}{\partial x} = \begin{pmatrix} u_2^T (\alpha_1 u_1 + \beta_1 v_1) & u_2^T (\alpha_1' u_1 + \beta_1' v_1) & -L_2 & -M_2 \\ v_2^T (\alpha_1 u_1 + \beta_1 v_1) & v_2^T (\alpha_1' u_1 + \beta_1' v_1) & -M_2 & -N_2 \\ u_2^T u_1 & u_2^T v_1 & -E_2 + g_N L_2 & -F_2 + g_N M_2 \\ v_2^T u_1 & v_2^T v_1 & -F_2 + g_N M_2 & -G_2 + g_N N_2 \end{pmatrix} \qquad (24)$$

One problem that has to be mentioned at this point is the variety of solutions. If one thinks e.g. of two spheres, there is an infinite number of solutions because of the periodicity of the sin and cos functions in the parametrization. Additional geometric considerations help here to find the correct point with shortest distance between the two bodies.

When the correct solution is found, the distance g_N between the possible contact points can be calculated as

$$g_N = n_1^T r_D = -n_2^T r_D, \quad r_D = r_{IG} + r_{GA} + r_{\Sigma 1} - r_{IB} - r_{\Sigma 2} \qquad (25)$$

The quantity g_N is then used as an indicator for the contact state. Its value is positive for 'no contact' and negative for penetration. We assume a point on surface 1 to be in contact with a corresponding point on surface 2, if their relative distance is smaller than a very small tolerance ε, $g_N < \varepsilon$.

5. Compliant Mating Parts

In this section we shall present two examples. The first one is an O-ring mounted on a piston to be inserted into a corresponding hole. The other are snap fasteners, which play an important role in automated assembly. The task is to find the correct relationship between the displacement and r_{IG} orientation A_{IG} of the gripper with respect to the environment and the forces f and moments m acting due to the deformation of the parts. For this purpose, we have to introduce an additional local frame L which is necessary to describe the deformation of the workpiece.

5.1. O-Ring

Figure 5 shows an elastic ring, mounted in a groove of a piston. It is inserted into a hole with a rounded chamfer at the beginning and at the end. This is a typical application of O-rings in hydraulic cylinders or pneumatic valves. In the hole there might be notches serving as an entrance or an outlet.
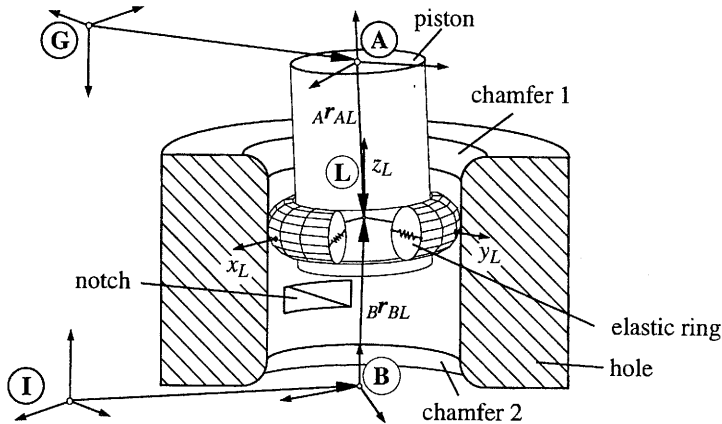

Fig. 5. O-ring in a groove on a piston.

An analytical solution for the stresses and strains in the elastic ring using approaches arising from continuum mechanics is not possible because the displacements and, in some instances, the material law are non-linear. Therefore we use a simplified approach, assuming the outer contour of the ring to be circular and rigid, so that there is a line contact between the ring and the hole. The only compliance taken into account is the radial stiffness of the O-ring, indicated by the small spring in Fig. 5. It is however not discrete, but continuously distributed over the circumference. Its

characteristics is supposed to be quadratic. The line load representing the elastic deformation of the ring is p_i. A further assumption is that the ring does not tilt in the hole, because orientational errors of industrial robots are generally small. According to the special geometry of the elastic ring in the groove, we use two contact line loads: one between the ring and hole p_a and one between the ring and groove p_o. Frictional loads $p_{a,R}$ and $p_{o,R}$ act perpendicularly to this normal loads and opposite the direction of relative motion in the contact line.

All further considerations are made in the **L**-frame which is placed at the height of the ring. It has a radial eccentricity e and a rotation φ_{BL} with respect to the **B**-frame. Its orientation is chosen such that its z-axis is parallel to the **B**-frame: $z_L \parallel z_B$ (because tilting is not regarded), and the x_L-axis coincides with the shortest stretch between the piston and hole. The eccentricity e, angle φ_{BL} and transformation matrix $\boldsymbol{A}_{BL}$ are defined as

$$e = \sqrt{{}_B r^2_{BL,x} + {}_B r^2_{BL,y}}, \qquad \varphi_{BL} = \arctan \frac{{}_B r_{BL,y}}{{}_B r_{BL,x}}$$

$$\boldsymbol{A}_{BL} = \begin{pmatrix} \cos \varphi_{BL} & \sin \varphi_{BL} & 0 \\ -\sin \varphi_{BL} & \cos \varphi_{BL} & 0 \\ 0 & 0 & 1 \end{pmatrix} \tag{26}$$

Through this special choice all further considerations can be made in two modelling planes, the x_L-y_L-plane shown in Fig. 6 on the left and the x_L-z_L-plane shown on the right. In the left part of the figure the line load p_a between the ring and the hole is drawn. The non-uniform distribution of the load can be clearly recognized.

The detection of the contact area is performed in the x_L-z_L-plane, where we then have to calculate the contact point between two circles, if the ring is entering or leaving the hole and touching one of the chamfers, or between a circle and a straight line, if the ring is inside the hole. For clarity, we have drawn the line loads acting between the bodies in the right modelling plane in Fig. 6.

If Δa is the deformation of the O-ring at the x_L-axis, then the deformation around the circumference $a(\varphi_L)$ is

$$a(\varphi_L) = \Delta a - e + e \cos \varphi_L \tag{27}$$

The line load representing the radial elasticity of the ring has the form:

$$p_i(\varphi_L) = c_1 a(\varphi_L) + c_2 a^2(\varphi_L) \tag{28}$$

where the coefficients c_1 and c_2 are the spring constants. They can be determined with a FEM calculation, where the cross-section of the elastic ring is radially deformed. From the resulting force-displacement-diagram the two coefficients are found by curve fitting. Inserting (27) in (28) yields

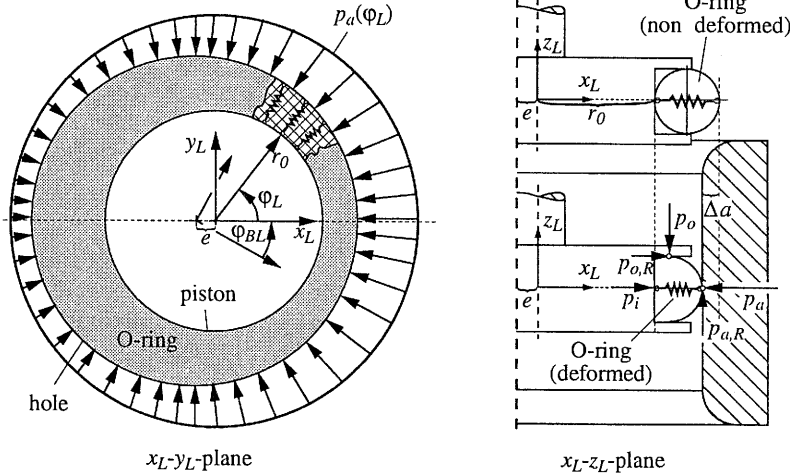$$p_i(\varphi_L) = k_0 + k_1 \cos \varphi_L + k_2 \cos^2 \varphi_L \tag{29}$$

Fig. 6. Two modelling planes for description of the mounting task with the O-ring.

with $k_0 = c_1 \left(\Delta a - \frac{e}{2} \right) + c_2 \left(\Delta a - \frac{e}{2} \right)^2$, $k_1 = c_1 \frac{e}{2} + c_2 e \left(\Delta a - \frac{e}{2} \right)$, $k_2 = c_2 \left(\frac{e}{2} \right)^2$. With this line load p_i and the other loads p_a, $p_{a,R}$, p_o and $p_{o,R}$ the force equilibrium at an infinitesimal ring segment is formulated. Solving the equilibrium for the outer load p_a yields

$$p_a(\varphi_L) = \frac{k_0 + k_1 \cos \varphi_L + k_2 \cos^2 \varphi_L}{1 - \mu^2} \tag{30}$$

if the ring is in the hole. Here μ is the coefficient of friction between rubber and steel. For the contact with the chamfers the equations are slightly different, because the changing direction of the loads has additionally to be taken into account. This load is split into three Cartesian directions of the L-frame:

$$p_x(\varphi_L) = -p_a(\varphi_L) \cos \varphi_L, \quad p_y(\varphi_L) = -p_a(\varphi_L) \sin \varphi_L, \quad p_z(\varphi_L) = \mu p_a(\varphi_L) \tag{31}$$

The resulting forces and moments acting on the origin of the L-frame are found through integration of p_x, p_y and p_z over the circumference of the ring:

$$_L\boldsymbol{f} = \begin{pmatrix} -2 \int\limits_0^\pi p_a(\varphi_L) \cos \varphi_L r_0 \, \mathrm{d}\varphi_L \\ -2 \int\limits_0^\pi p_a(\varphi_L) \sin \varphi_L r_0 \, \mathrm{d}\varphi_L \\ 2\mu \int\limits_0^\pi p_a(\varphi_L) r_0 \, \mathrm{d}\varphi_L \end{pmatrix}, \quad _L\boldsymbol{m} = \begin{pmatrix} 2\mu \int\limits_0^\pi p_a(\varphi_L) r_0^2 \cos \varphi_L \, \mathrm{d}\varphi_L \\ 2\mu \int\limits_0^\pi p_a(\varphi_L) r_0^2 \, \mathrm{d}\varphi_L \end{pmatrix} \tag{32}$$

where r_0 is the radius of the bolt inside the groove. These two loads are then transformed into the gripper system (G-frame), in order to combine the assembly

process with the robot model:

$$
\begin{pmatrix} {}_G f \\ {}_G m \end{pmatrix} = A_{GL} \begin{pmatrix} {}_L f \\ {}_L m + {}_L r_{GL} \times {}_L f \end{pmatrix}
\tag{33}
$$

To verify our model we present a comparison between the measurement and calculation. In the experiment a piston with a rubber ring 20×3.15 ($\varnothing$ 20 mm of the ring, $\varnothing$ 3.15 mm of the cross-section) was inserted into a hole of the diameter of 26 mm. For the specific material the spring constants are $c_1 = 16.0\,[\mathrm{N/mm^2}]$ and $c_2 = 43.0\,[\mathrm{N/mm^3}]$. This special experiment was conducted on a force measurement machine, which is very stiff, in order to avoid any disturbances from the manipulator. Thus we can assume ideal conditions. The force-distance graphs are shown in Fig. 7. The left diagram contains the measurement, and the right the calculations. The correspondence between both curves is very good. The maximum of the mating force arises when the ring is entering the hole. Inside the cylinder the load is constant.
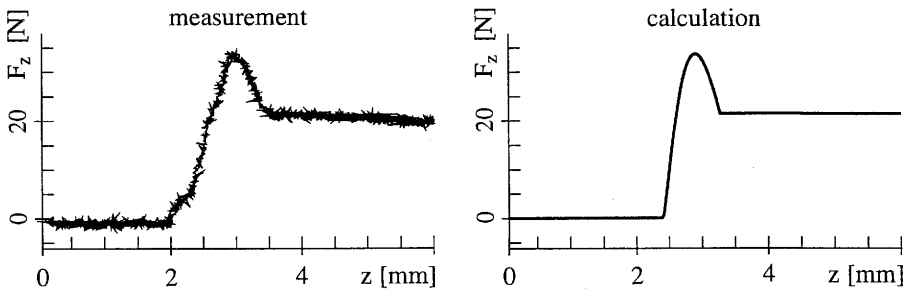
Fig. 7. Force-distance graph for O-ring insertion.

5.2. Snap Fastener

Snap fasteners are wide-spread fixtures in automated assembly. They consist of three different characteristic parts: the snap hook, the elastic support for the hook and the counterpart or chamfer. These parts can be seen in Fig. 8. The support consists of a beam (like in the figure), a plate or an even more complicated structure. We make the assumption that the snap hook and the chamfer are rigid and only the compliant support is flexible. We have to introduce a local L-frame, fixed to the snap hook, to describe the elasticity in the system. The deformations should be linear elastic, so that the vector ${}_A r_{AL} = (w_x, w_y, w_z)^T$ contains the displacement and the vector ${}_A \varphi_{AL} = (\varphi_x, \varphi_y, \varphi_z)^T$ represents the orientation between the A- and L-systems, expressed in the A-frame. With this description the compliance in the support can be reduced to a stiffness matrix K between the A- and the L-frame. This is symbolized by the spring in Fig. 8. Generally, the stiffness matrix K has dimension 6×6. The relationship between the linear deformations and the linear
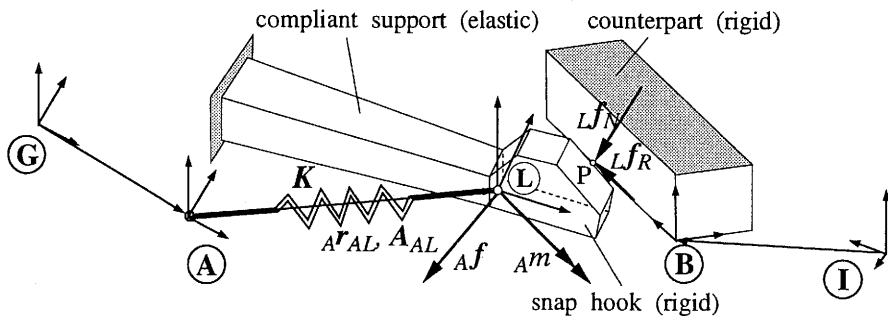
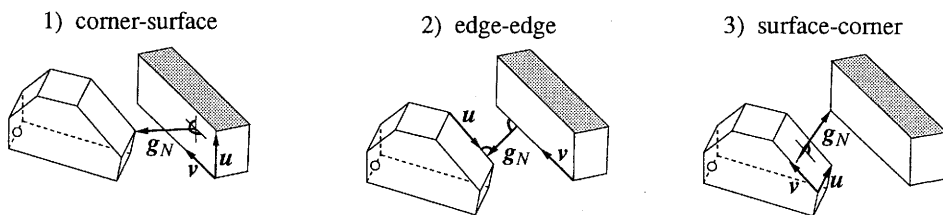Fig. 8. Basic structure of a snap fastener.

Fig. 9. Three different types of contact points between the snap hook and chamfer.

elastic reaction forces has the following form:

$$
\begin{pmatrix} {}_A f \\ {}_A m \end{pmatrix} = K \begin{pmatrix} {}_A r_{AL} \\ {}_A \varphi_{AL} \end{pmatrix} \qquad \in \mathbb{R}^6 \tag{34}
$$

where ${}_A f$ is the vector of the forces and ${}_A m$ is the vector of the torques acting at the origin of the L-frame when the deformations ${}_A r_{AL}$ and ${}_A \varphi_{AL}$ are imposed.

The description of the geometry is easy for the snap fasteners under consideration. The counterpart is a simple cuboid and the hook is a polygonal part with six corners. Thus there are three basic possibilities of contact points between the snap hook and counterpart as indicated in Fig. 9: corner-surface (type 1), edge-edge (type 2), and surface-corner (type 3). A contact between the flexible part and the counterpart is not taken into consideration. The location of a contact point is always indicated by two parameters u and v, which will be needed later in the equations of the force equilibrium.

When the snap hook and the counterpart get in contact, the parts will slide on each other and the hook will be displaced and twisted. In order to determine this movement and the necessary forces, we have to calculate the equilibrium position between these two parts. There is a force equilibrium between the elastic forces ${}_A f$ and ${}_A m$ on the one side and the contact forces ${}_L f_N$ and ${}_L f_R$ on the other side. The normal contact force ${}_L f_N$ acts on the touching point. Its direction depends on

the type of the contact. For type 1 and 3 (corner-surface) $_L f_N$ is normal to the plane, for type 2 (edge-edge) $_L f_N$ is parallel to the cross product of the two lines. The friction force $_L f_R$ acts perpendicularly to $_L f_N$ and opposite the direction of motion. For the formulation of the equilibrium, the forces have to be transformed into the same coordinate system, here the L-frame:

$$
\begin{pmatrix} A_{LA} & 0 \\ 0 & A_{LA} \end{pmatrix} \begin{pmatrix} {}_A f \\ {}_A m \end{pmatrix} = \begin{pmatrix} {}_L f_N +_L f_R \\ {}_L r_{LP} \times ({}_L f_N +_L f_R) \end{pmatrix} \tag{35}
$$

where $_L r_{LP}$ is the vector from the origin of the L-frame to the actual contact point P. A_{LA} is the transformation matrix between the A- and L-frame:

$$
A_{LA} = \begin{pmatrix} 1 & \varphi_z & -\varphi_y \\ -\varphi_z & 1 & \varphi_x \\ \varphi_y & -\varphi_x & 1 \end{pmatrix} \tag{36}
$$

Substituting (34) into (35) we obtain a system of six non-linear equations

$$
\begin{pmatrix} A_{LA} & 0 \\ 0 & A_{LA} \end{pmatrix} K \begin{pmatrix} {}_A r_{AL} \\ {}_A \varphi_{AL} \end{pmatrix} = \begin{pmatrix} {}_L f_N +_L f_R \\ {}_L r_{LP} \times ({}_L f_N +_L f_R) \end{pmatrix} \tag{37}
$$

The equations are rather complicated because of the multiplication by the transformation matrix. For the formulation we use the computer-algebra system MAPLE V. From the contact condition we obtain three additional equations, so that we have a set of nine non-linear algebraic equations. The unknowns are the six parameters for the position and the orientation of the hook: w_x, w_y, w_z, φ_x, φ_y, φ_z; two parameters for the contact between the parts: u, v; and the magnitude of the normal contact force $|_L f_N|$. Determining the mating forces has been described for one single contact. The problem can be solved for up to three touching points. For every additional contact we obtain three more equations from geometry and three additional unknowns: u_i, v_i and $|_L f_N|_i$. The system of non-linear equations has then dimension $\mathbb{R}^{6+3n}$, where n is the number of contacts, $n = 1, 2$ or 3. The transformation into the gripper system is again comparatively simple:

$$
\begin{pmatrix} {}_G f \\ {}_G m \end{pmatrix} = A_{GL} \begin{pmatrix} {}_L f_N +_L f_R \\ {}_L r_{GP} \times ({}_L f_N +_L f_R) \end{pmatrix} \tag{38}
$$

What is still missing is the determination of the stiffness matrix K representing the compliance in the parts. The elastic support can consist of a beam (Figs. 8 and 10) or a plate (Fig. 12). We apply beam and plate theory, respectively. We first regard the snap fastener from Fig. 10.
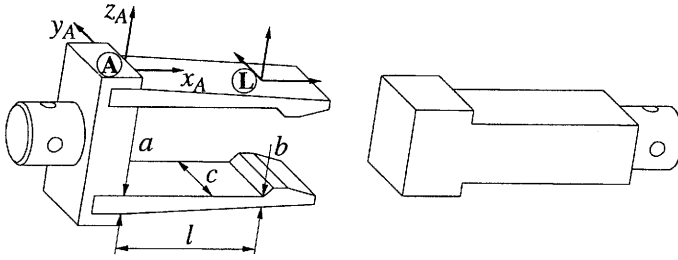
Fig. 10. Snap fastener with a beam as elastic support.

According to the picture the displacement in the x_A (w_x) and y_A (w_y) directions and the twist around the x_A (φ_x) and z_A (φ_z) axies are constrained. The stiffness in these directions would be very high compared with the other elements of K, therefore resulting in zeros in the first, second, fourth and sixth rows and columns. From beam theory (BERNOULLI-beam) the deflection curve is derived from the following differential equation:

$$EI_y(x)w_z'''(x) = -F_z, \qquad I_y(x) = \frac{1}{12}\left(a + \frac{x}{l}(b-a)\right)^3 c \tag{39}$$

The parameters a, b, c and l can be seen in Fig. 10 and E is the modulus of elasticity. Integrating (39) three times and using the boundary conditions $w_z(0) = 0$, $w_z'(0) = 0$ and $EI_y(l)w_z''(l) = -M_y$, yields a relationship between the displacement w_z, twisting φ_y ($\varphi_y = -w_z'(l)$) of the beam, force F_z and moment M_y. With $a = 5\,\text{mm}$, $b = 2.7\,\text{mm}$, $c = 20\,\text{mm}$, $l = 40\,\text{mm}$ and $E = 2700\,\text{N/mm}^2$ we obtain the following stiffness relationship:

$$\begin{pmatrix} F_x \\ F_y \\ F_z \\ M_x \\ M_y \\ M_z \end{pmatrix} = \begin{pmatrix} 0 & 0 & 0 & 0 & 0 & 0 \\ 0 & 0 & 0 & 0 & 0 & 0 \\ 0 & 0 & 45.5 & 0 & 638.8 & 0 \\ 0 & 0 & 0 & 0 & 0 & 0 \\ 0 & 0 & 638.8 & 0 & 14285.4 & 0 \\ 0 & 0 & 0 & 0 & 0 & 0 \end{pmatrix} \begin{pmatrix} w_x \\ w_y \\ w_z \\ \varphi_x \\ \varphi_y \\ \varphi_z \end{pmatrix} \tag{40}$$

Our model is again verified through a comparison between the measurement and calculation. Measurements were also made using the single axis force measurement machine. Figure 11 shows the force v. distance graph for the insertion of the upper half of the snap fastener from Fig. 10. F_x is the force in the direction of insertion and F_z acts perpendicularly. When mating the complete fitting with both parts, F_x becomes twice as large and F_z disappears because of the symmetry.

Our second example is a snap fastener with a plate as elastic support from Fig. 12. Here the displacement in the x_A (w_x) and y_A (w_y) direction and the twist around the z_A (φ_z) axis are constrained. Therefore K contains zeros in the first, second and sixth rows and columns. We assume a KIRCHHOFF plate. The bending is
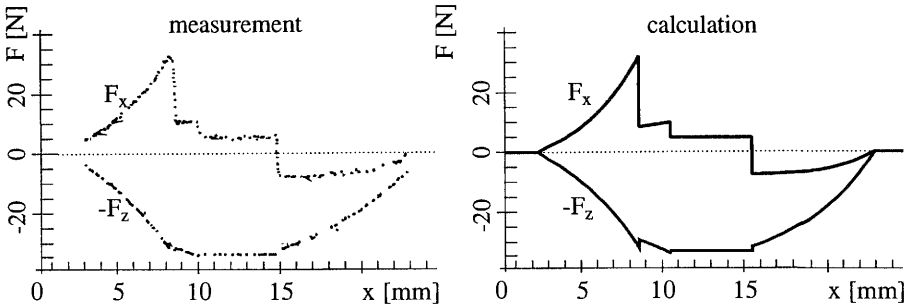
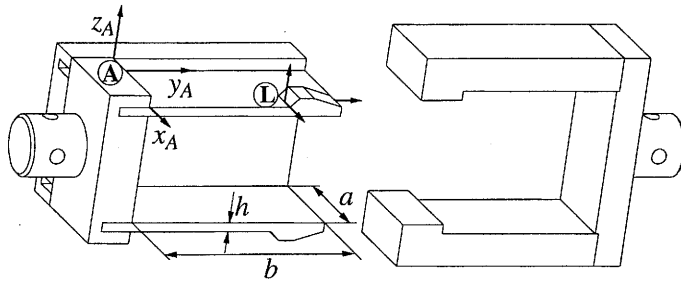Fig. 11. Force v. distance graph of snap fastener insertion.

Fig. 12 Snap fastener with a plate as elastic support.

approximated by a Ritz-series $w_z(x,y) = \boldsymbol{q}^T \boldsymbol{w}(x,y)$, with coordinates $\boldsymbol{q}$ and shape functions $\boldsymbol{w}$. As shape functions we use piecewise-defined cubic splines which satisfy the boundary conditions. The coordinates $\boldsymbol{q}$ of the shape functions are found by minimizing the potential $\Pi = W_i - W_a$. We then have to solve the variational problem: $(\partial \Pi / \partial \boldsymbol{q})^T = \boldsymbol{0}$, when W_i is the elastic energy in the plate:

$$
\begin{cases}
W_i = \dfrac{1}{2} D \, \boldsymbol{q}^T \int\limits_0^a \int\limits_0^b \boldsymbol{W}^T \begin{pmatrix} 1 & \nu & 0 \\ \nu & 1 & 0 \\ 0 & 0 & 2(1-\nu) \end{pmatrix} \boldsymbol{W} \, \mathrm{d}y \, \mathrm{d}x \, \boldsymbol{q} \\[2em]
D = \dfrac{Eh^3}{12(1-\nu^2)}, \quad \boldsymbol{W} = \left[\boldsymbol{w}_{,xx} | \boldsymbol{w}_{,yy} | \boldsymbol{w}_{,xy} \right]^T
\end{cases}
\tag{41}
$$

In the equations a, b and h describe the geometry of the plate according to Fig. 12, E is the modulus of elasticity and ν is Poisson's ratio. W_a is the work done by the loads F_z, M_x and M_y. Let x_L and y_L be the coordinates of the origin of the $\boldsymbol{L}$-frame:

$$
W_a = \left[F_z | M_x | M_y \right] \begin{pmatrix} \boldsymbol{w}^T(x_L, y_L) \\ \boldsymbol{w}_{,y}^T(x_L, y_L) \\ -\boldsymbol{w}_{,x}^T(x_L, y_L) \end{pmatrix} \boldsymbol{q}
\tag{42}
$$

After differentiating the potential with respect to q, we get a system of linear equations. Let $\widehat{q}$ be its solution. The dimension of the system depends on the number of shape functions we use. We then calculate the deformation of the point x_L, y_L using

$$
\begin{pmatrix} w_z \\ \varphi_x \\ \varphi_y \end{pmatrix} = \begin{pmatrix} \boldsymbol{w}^T(x_L, y_L) \\ \boldsymbol{w}^T_{,y}(x_L, y_L) \\ -\boldsymbol{w}^T_{,x}(x_L, y_L) \end{pmatrix} \widehat{q}
\tag{43}
$$

When $a = 32\,\text{mm}$, $b = 66\,\text{mm}$, $h = 3\,\text{mm}$, $E = 2700\,\text{N/mm}^2$, $\nu = 0.3$ and $x_L = 27\,\text{mm}$, $y_L = 48\,\text{mm}$, $\boldsymbol{K}$ is

$$
\begin{pmatrix} F_x \\ F_y \\ F_z \\ M_x \\ M_y \\ M_z \end{pmatrix} = \begin{pmatrix} 0 & 0 & 0 & 0 & 0 & 0 \\ 0 & 0 & 0 & 0 & 0 & 0 \\ 0 & 0 & 168.5 & -455.8 & 2105.1 & 0 \\ 0 & 0 & -455.8 & 26794.7 & -1443.3 & 0 \\ 0 & 0 & 2105.1 & -1443.3 & 37700.4 & 0 \\ 0 & 0 & 0 & 0 & 0 & 0 \end{pmatrix} \begin{pmatrix} u \\ v \\ w \\ \alpha \\ \beta \\ \gamma \end{pmatrix}
\tag{44}
$$

In Fig. 13 the results from the experiment and calculation are shown, for the insertion of the snap fastener from Fig. 12.
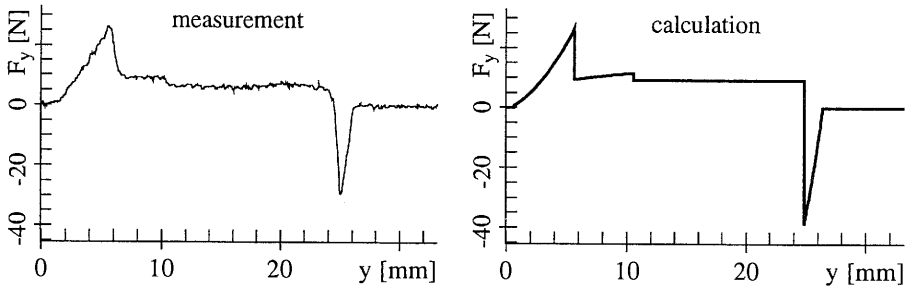
Fig. 13. Force v. distance graph of snap fastener insertion.

Altogether, we recognize a good correspondence between the theory and experiment for both cases. The force v. distance graphs show an unsteady shape because of the non-smooth contour of the snap hooks. It is also observed that the jumps in the mating force are sharper in the calculation than in the measurement. This results from local deformations of the snap hook especially when the contact forces become very high, e.g. at about 25 mm in Fig. 13.

6. Rigid Mating Parts

As regards rigid workpieces, where the deformation during assembly is very small, every contact point represents a constraint on the robot dynamics, which we shall

derive in the following. A constraint in the normal direction is the relative distance between two possible contact points. Its time derivative $\dot{g}_N$ is also needed:

$$g_N = n_1^T r_D \quad \Longrightarrow \quad \dot{g}_N = \dot{n}_1^T r_D + n_1^T \dot{r}_D \tag{45}$$

If we use the definitions from eqns. (25) and (20), we obtain:

$$\dot{g}_N = \left((\Omega_G \times n_1) + (\alpha u + \beta v)\dot{u}_1 + (\alpha' u + \beta' v)\dot{v}_1 \right)^T r_D$$
$$+ n_1^T \big(\underbrace{\dot{r}_{IG}}_{v_G} + \Omega_G \times \underbrace{(r_{GA} + r_{\Sigma 1})}_{r_{GC1}} + u_1 \dot{u}_1 + v_1 \dot{v}_1 - u_2 \dot{u}_2 - v_2 \dot{v}_2 \big) \tag{46}$$

This equation can be simplified if the conditions for a contact point in (23) are considered. All terms in the first line and most of the terms in the second line become then zero, and thus a simple expression remains:

$$\dot{g}_N = n_1^T v_{C1}, \qquad v_{C1} = v_G + \Omega_G \times r_{GC1} \tag{47}$$

The normal constraint is active if $g_N = 0$. Here v_{C1} is the velocity of the potential contact point on the upper body, which is connected to the gripper (see Fig. 4). In the two tangential directions a constraint is active if sticking occurs, which means that the relative sliding velocities $\dot{g}_U$ and $\dot{g}_V$ at a contact point are vanishing: $\dot{g}_U = 0$, $\dot{g}_V = 0$, where $\dot{g}_U$ and $\dot{g}_V$ are defined as the projections of v_{C1} on the two tangents u_1 and v_1, respectively:

$$\dot{g}_U = u_1^T v_{C1}, \qquad \dot{g}_V = v_1^T v_{C1} \tag{48}$$

In order to combine these constraint equations with the equations of motion of the manipulator, they are required on the acceleration level. Differentiating (45) and (48) once with respect to time yields

$$\ddot{g}_N = n_1^T \dot{v}_{C1} + \dot{n}_1^T v_{C1}$$
$$\ddot{g}_U = u_1^T \dot{v}_{C1} + \dot{u}_1^T v_{C1} \tag{49}$$
$$\ddot{g}_V = v_1^T \dot{v}_{C1} + \dot{v}_1^T v_{C1}$$

The time derivatives of the normal $\dot{n}_1$ and the tangents $\dot{u}_1$, $\dot{v}_1$ are defined as

$$\dot{n}_1 = \Omega_G \times n_1 + \frac{\partial n_1}{\partial u_1}\dot{u}_1 + \frac{\partial n_1}{\partial v_1}\dot{v}_1$$
$$\dot{u}_1 = \Omega_G \times u_1 + \frac{\partial u_1}{\partial u_1}\dot{u}_1 + \frac{\partial u_1}{\partial v_1}\dot{v}_1 \tag{50}$$
$$\dot{v}_1 = \Omega_G \times v_1 + \frac{\partial v_1}{\partial u_1}\dot{u}_1 + \frac{\partial v_1}{\partial v_1}\dot{v}_1$$

where the partial derivatives $\partial n_1/\partial u_1$, $\partial n_1/\partial v_1$, $\partial u_1/\partial u_1$, $\partial u_1/\partial v_1$, $\partial v_1/\partial u_1$, $\partial v_1/\partial v_1$ are known from eqns. (20)–(22). The velocity v_{C1} and thus its time derivative $\dot{v}_{C1}$ can be expressed depending on the generalized coordinates of the manipulator q, $\dot{q}$, because the body on which the point $C1$ is lying, is connected to the robot's gripper:

$$v_{C1} = v_G + \Omega_G \times r_{GC1} = J_T \dot{q} - \widetilde{r}_{GC1} J_R \dot{q} = J_{C1} \dot{q} \tag{51}$$

with J_{C1} being the translational Jacobian with respect to the contact point $C1$. The matrix $\widetilde{r}_{GC1}$ substitutes the cross-product: $\widetilde{r}_{GC1}\Omega_G = r_{GC1} \times \Omega_G$. Differentiating this equation yields

$$\dot{v}_{C1} = \dot{v}_G + \dot{\Omega}_G \times r_{GC1} + \Omega_G \times v_{C1} + \Omega_G \times (u_1 \dot{u}_1 + v_1 \dot{v}_1)$$

$$= \underbrace{(J_T - \widetilde{r}_{GC1} J_R)}_{J_{C1}} \ddot{q} + \underbrace{\left(\dot{J}_T - \widetilde{r}_{GC1} \dot{J}_R\right) \dot{q}}_{j_{C1}}$$

$$+ \Omega_G \times v_{C1} + \Omega_G \times (u_1 \dot{u}_1 + v_1 \dot{v}_1) \tag{52}$$

With the help of (50) and (6) we can rewrite (49) in the form

$$\ddot{g}_N = n_1^T \big(J_{C1} \ddot{q} + j_{C1} + \Omega_G \times v_{C1} + \Omega_G \times (u_1 \dot{u}_1 + v_1 \dot{v}_1)\big)$$
$$+ v_{C1}^T (\Omega_G \times n_1) + v_{C1}^T \big((\alpha_1 u_1 + \beta_1 v_1) \dot{u}_1 + (\alpha_1' u_1 + \beta_1' v_1) \dot{v}_1\big)$$

$$\ddot{g}_U = u_1^T \big(J_{C1} \ddot{q} + j_{C1} + \Omega_G \times v_{C1} + \Omega_G \times (u_1 \dot{u}_1 + v_1 \dot{v}_1)\big)$$
$$+ v_{C1}^T (\Omega_G \times u_1) + v_{C1}^T \big((\Gamma_{11,1}^1 u_1 + \Gamma_{11,1}^2 v_1 + L_1 n_1) \dot{u}_1$$
$$+ (\Gamma_{12,1}^1 u_1 + \Gamma_{12,1}^2 v_1 + M_1 n_1) \dot{v}_1\big) \tag{53}$$

$$\ddot{g}_V = v_1^T \big(J_{C1} \ddot{q} + j_{C1} + \Omega_G \times v_{C1} + \Omega_G \times (u_1 \dot{u}_1 + v_1 \dot{v}_1)\big)$$
$$+ v_{C1}^T (\Omega_G \times v_1) + v_{C1}^T \big((\Gamma_{12,1}^1 u_1 + \Gamma_{12,1}^2 v_1 + M_1 n_1) \dot{u}_1$$
$$+ (\Gamma_{22,1}^1 u_1 + \Gamma_{22,1}^2 v_1 + N_1 n_1) \dot{v}_1\big)$$

A simplification is possible if we substitute the constraints on the velocity level $\dot{g}_N$, $\dot{g}_U$ and $\dot{g}_V$ from eqns. (45) and (48) for the scalar products $v_{C1}^T n_1$, $v_{C1}^T u_1$ and $v_{C1}^T v_1$. We also know that $\dot{g}_N$ disappears when the normal constraint is active. The relative sliding velocities $\dot{g}_U$ and $\dot{g}_V$ vanish if the tangential constraints are active (stiction). The constraint equations have then the final form

$$\ddot{g}_N = \underbrace{n_1^T J_{C1}}_{w_N^T} \ddot{q}$$

$$+ \underbrace{n_1^T j_{C1} + n_1^T \big(\Omega_G \times (u_1 \dot{u}_1 + v_1 \dot{v}_1)\big) + \dot{g}_U (\alpha_1 \dot{u}_1 + \alpha_1' \dot{v}_1) + \dot{g}_V (\beta_1 \dot{u}_1 + \beta_1' \dot{v}_1)}_{\widetilde{w}_N}$$

$$\ddot{g}_U = \underbrace{u_1^T J_{C1}}_{w_U^T} \ddot{q} + \underbrace{u_1^T j_{C1} + u_1^T (\Omega_G \times v_1) \dot{v}_1}_{\widetilde{w}_U} \tag{54}$$

$$\ddot{g}_V = \underbrace{v_1^T J_{C1}}_{w_V^T} \ddot{q} + \underbrace{v_1^T j_{C1} + v_1^T (\Omega_G \times u_1) \dot{u}_1}_{\widetilde{w}_V}$$
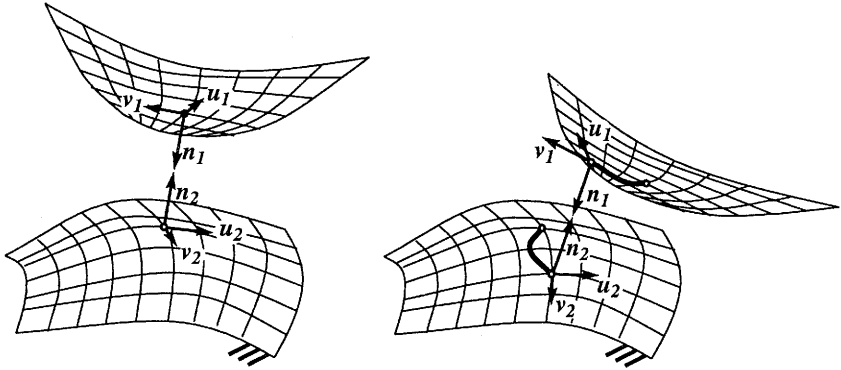
Fig. 14. Motion of the contact point on the surfaces.

The terms linearly dependent on the generalized accelerations $\ddot{q}$ are summarized in the constraint vectors w_N in the normal and w_U, w_V in the tangential direction. The remaining parts are abbreviated by using the scalar values $\widetilde{w}_N$, $\widetilde{w}_U$, $\widetilde{w}_V$.

The only unknowns in (54) are the time derivatives of the parameters $\dot{u}_1$, $\dot{v}_1$, $\dot{u}_2$, $\dot{v}_2$, which describe how the location of the contact point is moving on the two surfaces during the simulation. This situation is depicted in Fig. 14. To evaluate these derivatives we demand that the equations specifing the contact point eqn. (23) always have to be fulfilled. Their time derivatives have to disappear:

$$\frac{\mathrm{d}}{\mathrm{d}t}\left(n_1^T u_2\right) = 0, \qquad \frac{\mathrm{d}}{\mathrm{d}t}\left(n_1^T v_2\right) = 0, \qquad \frac{\mathrm{d}}{\mathrm{d}t}\left(r_D^T u_2\right) = 0, \qquad \frac{\mathrm{d}}{\mathrm{d}t}\left(r_D^T v_2\right) = 0 \quad (55)$$

We conclude from (55) a system of equations which are linear in the derivatives of the contour parameters:

$$\begin{pmatrix} u_2^T(\alpha_1 u_1 + \beta_1 v_1) & u_2^T(\alpha_1' u_1 + \beta_1' v_1) & L_2 & M_2 \\ v_2^T(\alpha_1 u_1 + \beta_1 v_1) & v_2^T(\alpha_1' u_1 + \beta_1' v_1) & M_2 & N_2 \\ -u_1^T u_2 & -u_1^T u_2 & E_2 & F_2 \\ -u_1^T v_2 & -u_1^T v_2 & F_2 & G_2 \end{pmatrix} \begin{pmatrix} \dot{u}_1 \\ \dot{v}_1 \\ \dot{u}_2 \\ \dot{v}_2 \end{pmatrix} = \begin{pmatrix} -\Omega_1^T(u_2 \times n_1) \\ -\Omega_1^T(v_2 \times n_1) \\ u_2^T v_{C1} \\ v_2^T v_{C1} \end{pmatrix} \quad (56)$$

This linear problem has to be solved at every time step of numerical integration.

More than one sliding or sticking contact point between mating parts, may exist so that a variable number of constraints is active during the simulation. Let n_n be the number of contact points and n_T the number of sticking contact points. Then the constraint equations in vector form are

$$\begin{cases} \ddot{g}_N = W_N^T \ddot{q} + \widetilde{w}_N \\ \ddot{g}_U = W_U^T \ddot{q} + \widetilde{w}_U \\ \ddot{g}_V = W_V^T \ddot{q} + \widetilde{w}_V \end{cases} \quad (57)$$

where

$$W_N = (w_{N,1}, \ldots, w_{N,n_N}) \in \mathbb{R}^{f,n_N}, \quad \widetilde{w}_N = (\widetilde{w}_{N,1}, \ldots, \widetilde{w}_{N,n_N})^T \in \mathbb{R}^{n_N}$$

$$W_U = (w_{U,1}, \ldots, w_{U,n_T}) \in \mathbb{R}^{f,n_T}, \quad \widetilde{w}_U = (\widetilde{w}_{U,1}, \ldots, \widetilde{w}_{U,n_T})^T \in \mathbb{R}^{n_T}$$

$$W_V = (w_{V,1}, \ldots, w_{V,n_T}) \in \mathbb{R}^{f,n_T}, \quad \widetilde{w}_V = (\widetilde{w}_{V,1}, \ldots, \widetilde{w}_{V,n_T})^T \in \mathbb{R}^{n_T}$$

They are combined with the equations of motion and thus form a system of differential-algebraic equations

$$M\ddot{q} = \widehat{h} + (W_N + W_F)\lambda_N + W_U\lambda_U + W_V\lambda_V \tag{58}$$

$$\underbrace{\begin{pmatrix} \ddot{g}_N \\ \ddot{g}_N \\ \ddot{g}_N \end{pmatrix}}_{\ddot{g}} = \underbrace{\begin{pmatrix} W_N^T \\ W_U^T \\ W_V^T \end{pmatrix}}_{W^T} \ddot{q} + \underbrace{\begin{pmatrix} \widetilde{w}_N \\ \widetilde{w}_U \\ \widetilde{w}_V \end{pmatrix}}_{\widetilde{w}} \tag{59}$$

with $\widehat{h} = h + Bu - P\dot{q} - Qq$. The components of the vectors $\lambda_N = (\lambda_{N,1}, \ldots, \lambda_{N,n_N})^T$, $\lambda_U = (\lambda_{U,1}, \ldots, \lambda_{U,n_T})^T$ and $\lambda_V = (\lambda_{V,1}, \ldots, \lambda_{V,n_T})^T$ correspond to the unknown constraint forces normal and tangential to the respective tangent plane. The term $W_F\lambda_N$ considers frictional forces in all contact points where sliding occurs. The direction is given by the velocity of the contact point v_{C1} shown in Fig. 15, and the magnitude by the normal contact force λ_N. The vector v_{C1} can be split into two tangential directions, which are assumed to be perpendicular:

$$v_{C1} = \frac{u_1^T v_{C1}}{u_1^T u_1} u_1 + \frac{v_1^T v_{C1}}{v_1^T v_1} v_1 \Longrightarrow v_{C1} = \frac{\dot{g}_U}{E_1} u_1 + \frac{\dot{g}_V}{G_1} v_1, \quad |v_C| = \sqrt{\frac{\dot{g}_U^2}{E_1} + \frac{\dot{g}_V^2}{G_1}} \tag{60}$$

The vector of the friction force f_R at a sliding contact point is then defined as (see also Fig. 15)

$$f_R = -\frac{v_{C1}}{|v_{C1}|} \mu\lambda_N = u_1 \frac{-\mu\dot{g}_U\lambda_N}{E_1\sqrt{\dfrac{\dot{g}_U^2}{E_1} + \dfrac{\dot{g}_V^2}{G_1}}} + v_1 \frac{-\mu\dot{g}_V\lambda_N}{G_1\sqrt{\dfrac{\dot{g}_U^2}{E_1} + \dfrac{\dot{g}_V^2}{G_1}}}$$

$$= \left(u_1 \frac{\dot{g}_U}{E_1} + v_1 \frac{\dot{g}_V}{G_1}\right) \frac{-\mu\lambda_N}{\sqrt{\dfrac{\dot{g}_U^2}{E_1} + \dfrac{\dot{g}_V^2}{G_1}}} \tag{61}$$

The projection of f_R onto the generalized coordinates is realized through the multiplication by the Jacobian with respect to the contact point J_{C1}:

$$w_F = J_{C1}^T \left(u_1 \frac{\dot{g}_U}{E_1} + v_1 \frac{\dot{g}_V}{G_1}\right) \frac{-\mu\lambda_N}{\sqrt{\dfrac{\dot{g}_U^2}{E_1} + \dfrac{\dot{g}_V^2}{G_1}}} = \left(w_U \frac{\dot{g}_U}{E_1} + w_V \frac{\dot{g}_V}{G_1}\right) \frac{-\mu\lambda_N}{\sqrt{\dfrac{\dot{g}_U^2}{E_1} + \dfrac{\dot{g}_V^2}{G_1}}} \tag{62}$$
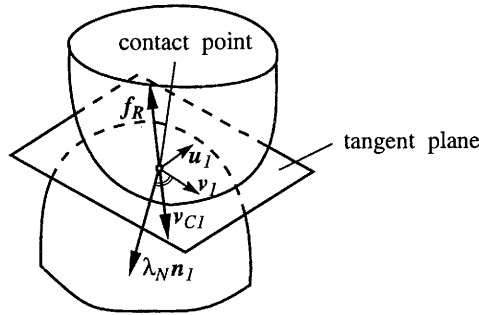
Fig. 15. Direction of the sliding forces $\boldsymbol{f}_R$ in the tangential plane between two contact points.

The matrix $\boldsymbol{W}_F$ is then composed of the sliding constraint vectors $\boldsymbol{w}_F$ defined above. At the contact point where friction occurs the elements $\boldsymbol{w}_F$ are zero:

$$\boldsymbol{W}_F = (\boldsymbol{w}_{R,1}, \ldots, \boldsymbol{w}_{R,n_N}) \in \mathbb{R}^{f,n_N} \tag{63}$$

The systems of differential-algebraic equations (58) and (59) can be easily solved if all active constraints are known and do not change, i.e. $\ddot{\boldsymbol{g}} = 0$. We solve eqn. (58) for the accelerations $\ddot{\boldsymbol{q}}$ and insert them into the algebraic equation (59):

$$\underbrace{\boldsymbol{W}^T \boldsymbol{M}^{-1}\left((\boldsymbol{W}_N + \boldsymbol{W}_F)|\boldsymbol{W}_U|\boldsymbol{W}_V\right)}_{\boldsymbol{A}} \begin{pmatrix} \lambda_N \\ \lambda_U \\ \lambda_V \end{pmatrix} + \underbrace{\boldsymbol{W}^T \boldsymbol{M}^{-1}\widehat{\boldsymbol{h}} + \widetilde{\boldsymbol{w}}}_{\boldsymbol{b}} = 0 \tag{64}$$

This system of linear equations has to be solved at every time step of numerical integration to evaluate the constraint forces. They are then inserted into the constrained equations of motion (58) to simulate the robot in contact with the environment.

Special treatment is necessary if the constraints are changing during the insertion. For this purpose, we have defined special indicators that notify a transition in the state of a the contact points. The resulting sliding velocity in the tangential plane at the contact point is $\dot{g}_T = |\boldsymbol{v}_{C1}| = \sqrt{(\dot{g}_U^2/E) + (\dot{g}_V^2/G)}$. A summary of all indicators and possible transitions is shown in the following table:

constraint	change	indicator	typ of indicator
getting active	no contact $\rightarrow$ contact	$g_N = 0$	kinematic
	sliding $\rightarrow$ sticking	$\dot{g}_T = 0$	
getting passive	contact $\rightarrow$ no contact	$\ddot{g}_N > 0$	kinetic
	sticking $\rightarrow$ sliding	$\ddot{g}_T > 0$	

A change in the topology of the system due to a change in the constraints causes the velocity, acceleration and constraint force in the specific contact point to be unsteady, especially if stick-slip phenomena or impacts occur. One method for finding a solution consistent with the dynamic constraints is a combinatorial search, where all combinations of constraints have to be tested. With an increasing number of possible contact points the combinatorial approach, however, is very time-consuming in computation. More effective methods are the application of an iterative algorithm in the general spatial case, or the formulation of the contact laws as a Linear Complementarity Problem (LCP) in the planar case. The iterative method is described in detail in (Pfeiffer and Glocker, 1996; Wösle and Pfeiffer, 1996). The definition of the LCP for assembly processes can be found in (Pfeiffer and Glocker, 1996; Seyfferth, 1993).

6.1. Round Peg and Hole

The experimental setup with PUMA, environment and sensors is shown in Fig. 16. The force-torque sensor between the last joint of the manipulator and the gripper is used to measure the mating forces. The six laser sensors are utilized to observe the position and orientation of the gripper. In this setup the peg was cylindrical with a diameter of ⌀ 39.9 mm and a round chamfer of the radius $r_1 = 4$ mm, shown in Fig. 17. The hole had a diameter of ⌀ 40 mm and also a round chamfer of the radius $r_2 = 6$ mm. Thus the clearance between the peg and the hole is only 0.1 mm. Mathematically, the peg and the hole are cylinders, each chamfer is modelled as a torus. The parametrization of the peg is e.g.

$$\text{cylinder: } r_{\Sigma 1} = \begin{pmatrix} R_1 \cos u_1 \\ R_1 \sin u_1 \\ v_1 \end{pmatrix}, \quad \text{torus: } r_{\Sigma 1} = \begin{pmatrix} (R_1 + r_1(\cos v_1 - 1)) \cos u_1 \\ (R_1 + r_1(\cos v_1 - 1)) \sin u_1 \\ \sin v_1 \end{pmatrix} \quad (65)$$

where $R_1 = 19.95$ mm and $r_1 = 4.0$ mm. The description of the hole is the same, we only have to replace the index $(\cdot)_1$ by the index $(\cdot)_2$, where $R_2 = 20.0$ mm and $r_2 = 6.0$ mm. Between the two mating partners three potential contact points exist:

number	peg		hole
1	torus 1	⟷	torus 2
2	cylinder 1	⟷	torus 2
3	torus 1	⟷	cylinder 2

The position of the robot for the insertion task was $\gamma_0 = (-8.4°, -152.8°, 17.9°, 0.0°, -44.9°, -8.4°)^T$. The initial displacement of the robot with respect to the axis of the hole was 2.1 mm in the x_G-direction and 1.3 mm in the y_G-direction (see G-frame in Fig. 16 for detailed explanation). The mating trajectory was 80 mm along the z_G-axis. In Fig. 17 we see the first results from the insertion. The peg and hole are displayed from two sides. A trace of contact points can be seen on the parts. On the left we recognize the point of the first contact between the two
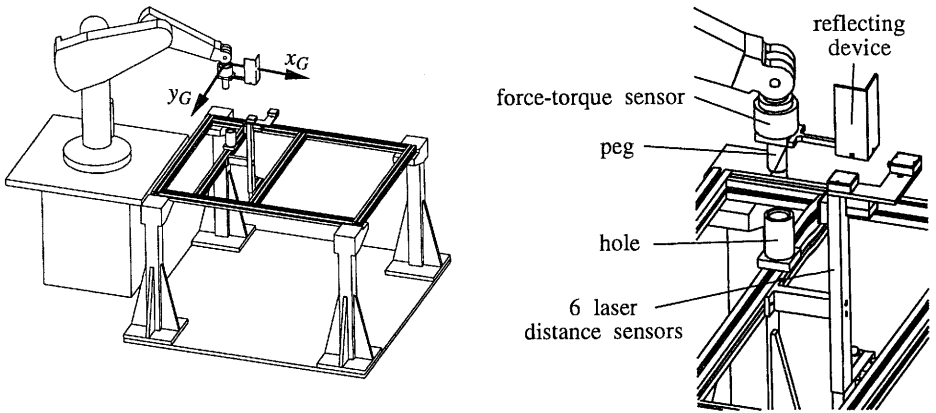
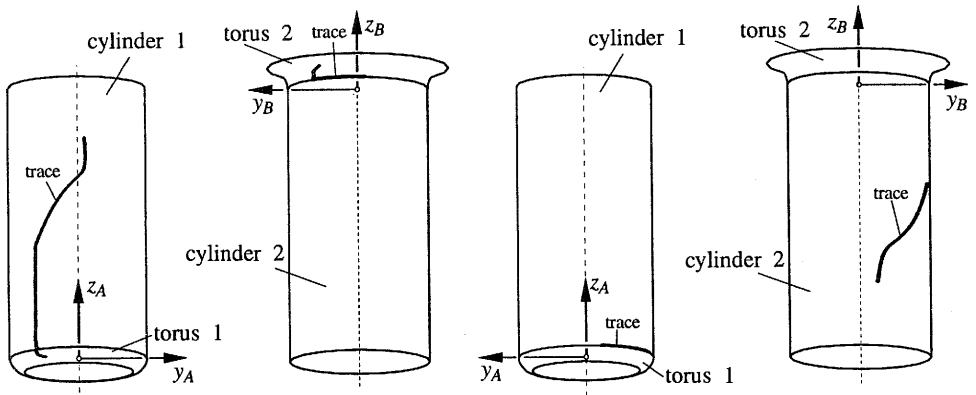Fig. 16. Experimental setup for mating experiments.

Fig. 17. Trace of the contact points on the mating parts.

chamfers, due to the initial displacement. The workpieces are then sliding along the chamfers, until there is a transition of the contact point to the cylinder of the peg. In this situation, the peg touches the chamfer along a straight line, as long as only one point is in contact. After about 5 cm of insertion, a second contact point arises on the other side, shown in Fig. 17 on the right. Through this additional constraint the peg is moving in such a way that both contact points are moving to the middle of the peg with respect to the displayed viewpoint. In Fig. 18 we have demonstrated the constraint forces of the three possible contact-point combinations, which prevent the parts from penetrating each other. In the left diagram we recognize that the force between the two chamfers is relatively small. As the two chamfers lose contact, the force is transferred by the next constraint between cylinder$_1$ and torus$_2$. When the second contact point arises, at about 1.3 s, the load starts rising. As the peg moves deeper into the hole, two opposing forces are acting at different sides of the peg, achieving values of more than 100 N. In Fig. 19 we finally present the mating
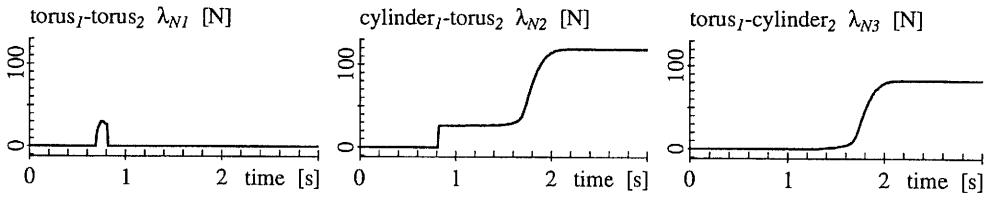
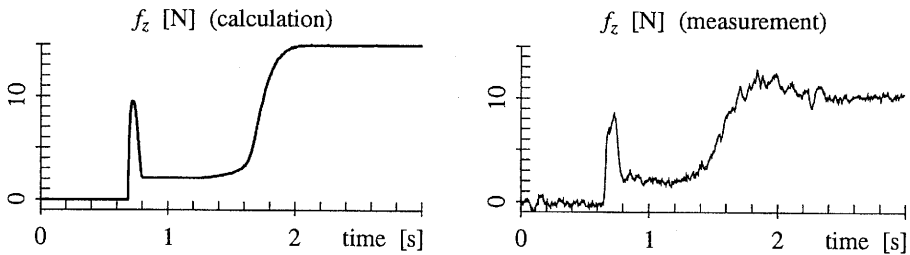Fig. 18. Constraint forces between the contact points.

Fig. 19. Mating force f_z in direction of insertion.

force in the direction of insertion. Here we can show both the measurement and calculation. Even though the contact forces reach very large values, the mating forces remain on a lower level. At the beginning we see clearly a peak when the two chamfers get in contact. As only one constraint is active, the load is low afterwards. The largest values appear again in the two-point contact situation. But they do not rise to such a high level as the contact forces themselves, because the latter act in different directions. This part of the insertion is mainly governed by friction between the parts. Concluding we can summarize that the correspondence between the calculation and measurement is good, as shown in Fig. 19.

6.2. Rectangular Peg and Hole

Finally, we consider a rectangular peg with a chamfer inserted into a rectangular hole, where the geometry is shown in Fig. 20 on the left. If we introduce four modelling planes, we can reduce this spatial example to a planar description, which makes the computation faster due to another algorithm (LCP). On every side of the peg one such plane is introduced, which is displayed in Fig. 20 on the right. Two sides are situated within the xy-plane, and two in the xz-plane. There are two different types of contact points: point-plane and edge-edge. Let the letters a, b, c, d in Fig. 20(b) denote points and the numbers $1', 2', 3', 4', 5'$ denote planes. Then there are four possible contact points of the type point-plane: $a - 2'$, $b - 1'$, $c - 5'$, $d - 4'$. For the type edge-edge the numbers $1, 2, 3, 4, 5$ denote edges on the peg and the letters a', b' denote edges of the hole. There exist six potential contacts of this type: $1 - a'$, $2 - a'$, $3 - a'$, $3 - b'$, $4 - b'$, $5 - b'$. Thus we have altogether 40 potential constraints between the peg and the hole with the sketched geometry in the spatial case.
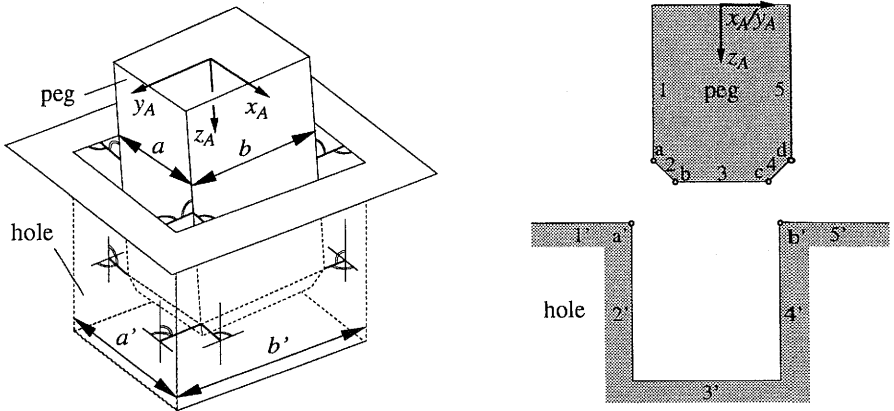
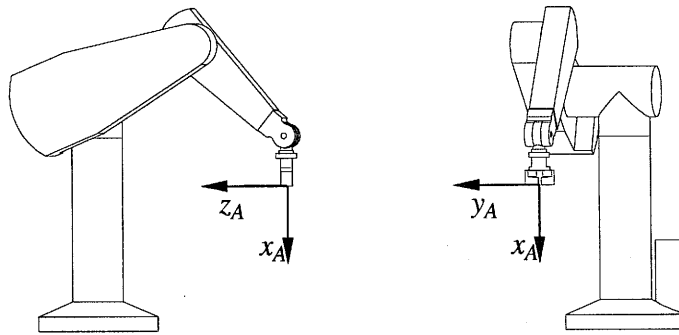Fig. 20. Geometry of the rectangular peg and hole.

Fig. 21. Position of the manipulator for the insertion of the rectangular peg.

Measurements were again conducted with the PUMA 560 manipulator inserting the rectangular peg with the chamfer into the rectangular hole. The starting position of the manipulator was $\gamma_0 = (4.6°, -157.2°, 27.5°, 0.0°, -50.3°, 4.6°)^T$, which is shown in Fig. 21 from two sides. The equations of motion of the robot were linearized around this working point. The mating parts can be seen in Fig. 20, where the peg had the measures $a = 45.2\,\text{mm}$, $b = 45.4\,\text{mm}$ with a chamfer $45° \times 4\,\text{mm}$ and the hole had the dimensions $a' = 46.0\,\text{mm}$, $b' = 45.8\,\text{mm}$. The robot's path during the mating task was $80\,\text{mm}$ in the positive x_A-direction. We show here the results of four experiments compared with numerical simulations. The initial lateral displacement between the peg and the hole was set to $\pm 4\,\text{mm}$ in the two Cartesian directions y_A and z_A.

Displacement in the y-direction

Let us consider first the experiments, where the displacement was $\Delta y_A = \pm 4\,\text{mm}$. In Fig. 22 the gripper forces during insertion F_x and F_y are shown. The upper plots are measurements, the lower plots are the calculated results for the same starting

a) displacement $\Delta y_A = 4$mm   b) displacement $\Delta y_A = -4$mm
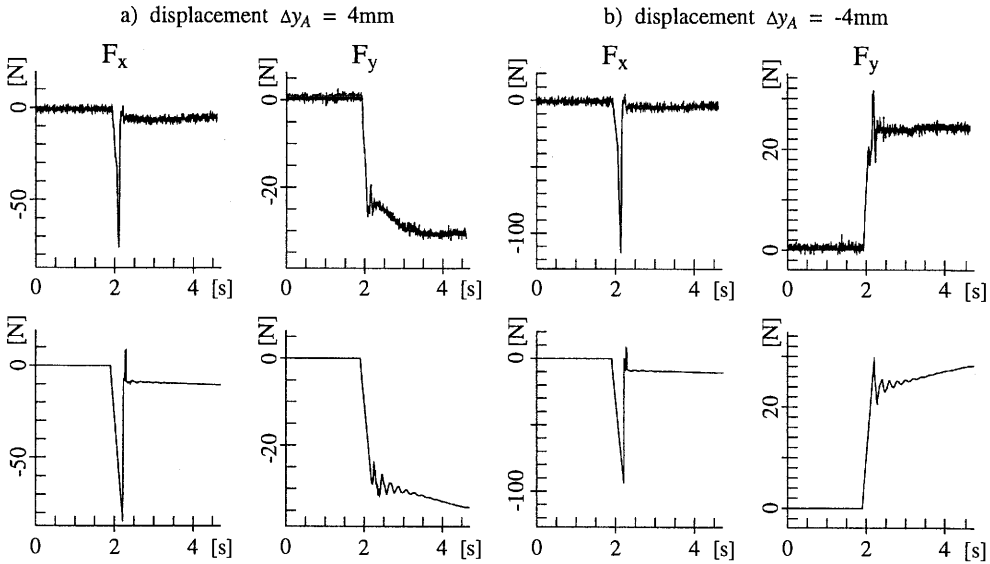

Fig. 22. Mating forces for displacement in the y_A direction (top: measurements, bottom: calculations).

configuration. In both cases there is a peak of F_x versus the manipulator motion, when the chamfer of the peg comes in contact with the upper edge of the hole (see Fig. 20 on the right, contact points of type $4 - b'$ in the case of the positive or $2 - a'$ in the case of the negative displacement). After having passed the edge, it is sliding downwards, having contact with one side of the hole (see Fig. 20, contact points of type $5 - b'$ in the case of the positive or $1 - a'$ in the case of the negative displacement). The force F_y due to this contact acts towards the centre of the hole.

Displacement in the z-direction

More interesting are the experiments, where the displacement was varied in the z_A-direction: (a) $\Delta z_A = +4$ mm, (b) $\Delta z_A = -4$ mm. Here the behaviour of the manipulator is different for both cases, see Fig. 23 (top: measurement, bottom: calculation). If there is a displacement $\Delta z_A = +4$ mm, there is again a force peak in F_x at the first contact (contact points of type $4 - b'$), when the chamfer slides at the upper edge of the hole. The peg is then sliding into the hole, having contact with the upper edge $(5 - b')$, as is the case in the first two experiments. A completely different behaviour can be observed when the lateral displacement is $\Delta z_A = -4$ mm. Here only the beginning of the insertion is similar to the other cases $(2 - a'$ and $1 - a')$. But as the peg proceeds deeper into the hole, there are additional contact points (of type $d - 4'$) inside the hole after about 2.7 s. The contact forces and thus the mating forces F_x and F_z become very large because jamming occurs. The insertion finally succeeds on account of the fact that drive torques are increased by the controller.

The reason for the unsymmetric behaviour of the robot in cases (a) and (b) can be found in the robot's starting configuration shown in Fig. 21. If a force in the
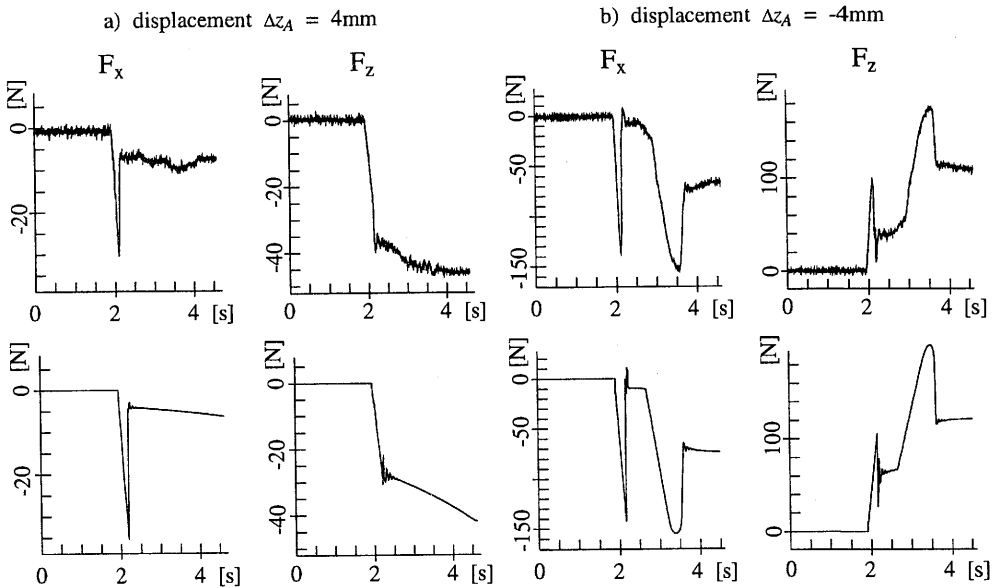
Fig. 23.   Mating forces for displacement in the z_A-direction (top: measurements, bottom: calculations).

negative x_A-direction is applied, the manipulator is not only displaced in the same direction $(-x_A)$, but also in the negative z_A-direction because of couplings in the stiffness matrix. This means for the example with the initial displacement $\Delta z_A = +4\,\text{mm}$ (Fig. 23(a)) that the gripper is moved towards the centre of the hole, when the peg is in contact with the hole. Therefore the contact forces are reduced. The opposite happens if the lateral displacement is $\Delta z_A = -4\,\text{mm}$. As mating forces act on the gripper, the gripper moves away from the hole, whereas the mating forces additionally increase.

7. Combined Assembly Process

Finally, we investigate a combined assembly process, consisting of a flexible part on one side and a rigid body on the other side. As can be seen in Fig. 24, two bolts, one rectangular bolt and the other round with an O-ring mounted on it, were inserted into the corresponding holes. The experiment was made for two different positions shown in Fig. 24, which are called Position 1 and Position 2. For each insertion numerical simulations were made.

Figure 25 contains measured and calculated results for both positions, on the left for Position 1, and on the right for Position 2. The first two curves on both sides are the measured and calculated mating forces. They have nearly the same values for both positions. Great differences for the two locations can be observed in the last three curves which show the Cartesian velocity of the gripper in the direction of insertion. As a basic characteristic, the trapozoid velocity profile from the VAL II controller can
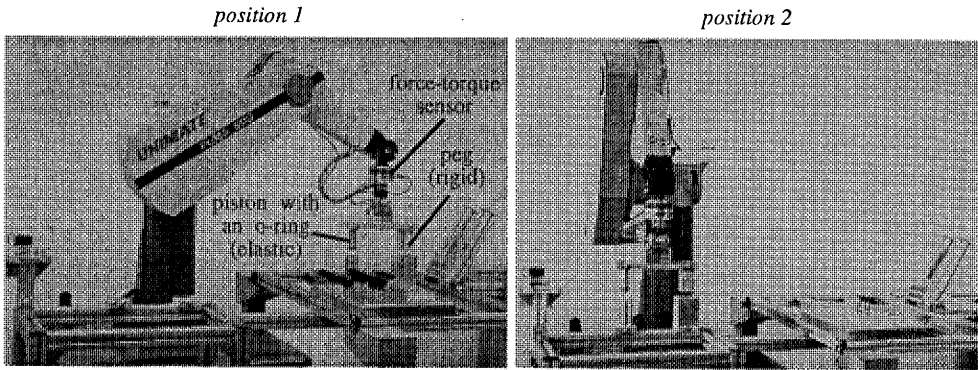
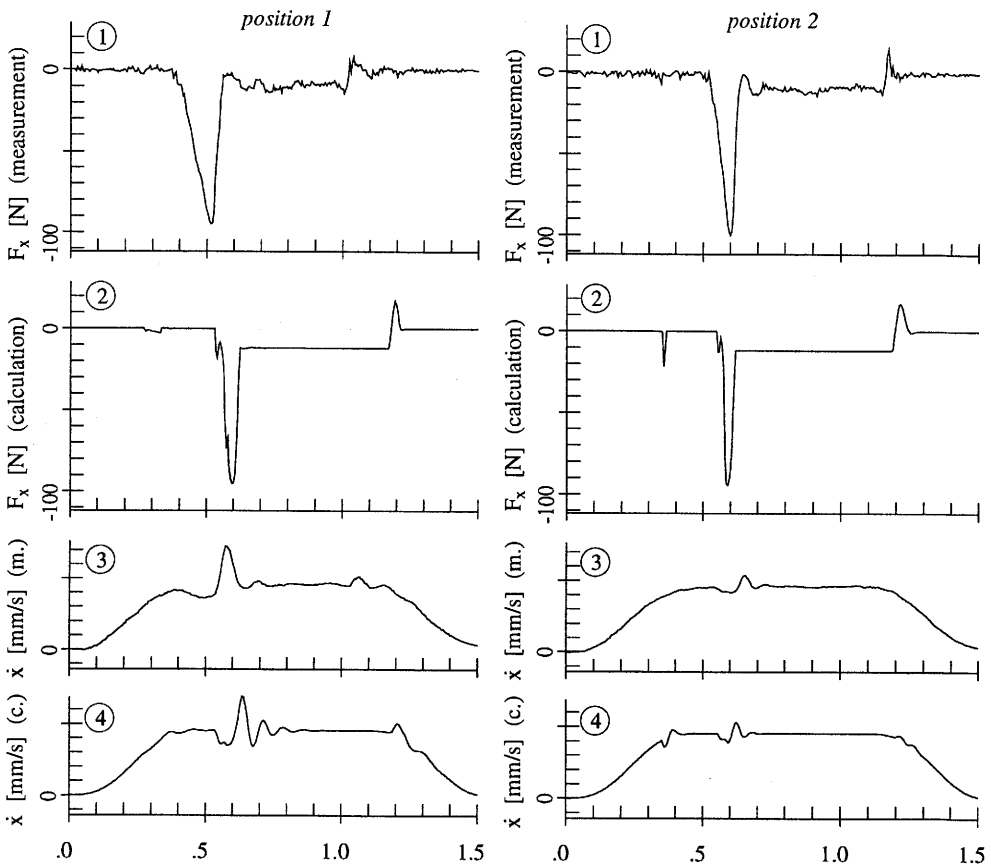Fig. 24. Two locations for the experiment with a combined assembly task.

Fig. 25. Measurement and calculation of the mating force and Cartesian velocity
        for both positions.

be noticed. Additionally, oscillations can be seen very well on the velocity plot. For both locations, the velocity of the gripper decreases when the magnitude of the mating force reaches its maximum, due to the deformation of the O-ring, when entering the cylindrical hole. Once the O-ring is in the hole, the load decreases drastically. The manipulator is excited to an overshot, which is however larger for Position 1. When the ring is leaving the hole, similar effects occur. They are not so strong, because the changes in the force characteristic are smaller. We can conclude that Position 2 is much more suitable for this mating process, because the manipulator deviates less from the ideal velocity at this location. The insertion proceeds more smoothly.

Another phenomenon is the influence of impacts. In both simulations impacts occurred when the rectangular peg had the first contact with the corresponding hole (at about 0.35 s). The effect of the impact is stronger for Position 2 because the robot is stiffer here. The resulting oscillation however is very short and of a smaller amplitude than that caused by the mating forces.

8. Conclusion

A method was presented to model a robot performing an assembly task, where both the robot dynamics and contact mechanics between the mating parts are considered. The workpieces might be elastic or rigid, which requires different approaches. The comparison between measured and calculated results shows that our methods are capable of describing mating tasks with flexible and rigid workpieces executed by a robot. All important effects that show up in the experiment are covered by the simulation. Thus we are capable of predicting the behaviour of the robot as well as the load on the parts by numerical simulations. The aim is to recognize and avoid problems with the automated part-mating process in advance and thus save time and money.

Acknowledgment

References

Asada H. and Kakumoto Y. (1988): *The dynamic RCC hand for high-speed assembly.* — Proc. IEEE Conf. *Robotics and Automation*, Philadelphia, PA, pp.120–125.

Bergqvist C., Söderquist B. and Wernerson Å. (1994): *On combining accelerometers, force/torque-sensors, and electrical sensing for detecting contact errors during assembly.* — Proc. IEEE/RSJ Int. Conf. *Int. Robots and Systems*, Munich, Germany, pp.1736–1743.

Bronstein I.N. and Semendjajew K.A. (1985): *Taschenbuch der Mathematik.* — Thun: Verlag Harri Deutsch.

Bruyninckx H., Dutré S. and De Schutter J. (1995): *Peg-on-hole: A model based solution to peg and hole alignment.* — Proc. IEEE Conf. *Robotics* and *Automation*, Nagoya, Japan, pp.1919–1924.

Caine M. E., Lozano-Pérez T. and Seering W.P. (1989): *Assembly strategies for chamferless parts.* — Proc. IEEE Conf. *Robotics* and *Automation*, Scottsdale, AZ, pp.472–477.

Donald B. and Pai D. (1990): *On the motion of compliantly-connected rigid bodies in contact, part II: A system for analyzing designs for assembly.* — Proc. IEEE Conf. *Robotics* and *Automation*, Cincinatti, OH, pp.2708–2715.

Farahat A.O., Graves B.S. and Trinkle J.C. (1995): *Identifying contact formations in the presence of uncertainty.* — Proc. IEEE/RSJ Conf. *Int. Robots* and *Systems*, Pittsburgh, PA, Vol.3, pp.59–64.

Gottschlich S.N. and Kak A.C. (1988): *A dynamic approach to high-precision parts mating.* — Proc. IEEE Conf. *Robotics* and *Automation*, Philadelphia, PA, pp.1246–1253.

Jennings J., Donald B. and Campbell D. (1989): *Towards experimental verification of an automated compliant motion planner based on a geometric theory of error detection and recovery.* — Proc. IEEE Conf. *Robotics* and *Automation*, Scottdale, AZ, pp.632–637.

Johanni R. (1987): *On the automatic generation of the equations of motion for robots with elastically deformable arms.* — Prep. IFAC/IFIP/IMACS Int. Symp. *Theory of Robots*, Vienna, Austria.

Lozano-Perez T., Mason M.T. and Taylor R.H. (1984): *Automatic synthesis of fine-motion strategies for robots.* — Int. J. Robotics Research, Vol.3, No.1.

McCarragher B. and Asada H. (1992): *A discrete event controller using Petri nets applied to assembly.* — Proc. IEEE/RSJ Int. Conf. *Int. Robots* and *Systems*, Rayleigh, NC, pp.2087–2094.

Meitinger Th. and Pfeiffer F. (1994): *Automated assembly with compliant mating parts.* — Proc. IEEE Conf. *Robotics* and *Automation*, San Diego, CA, pp.1462–1467.

Meitinger Th. and Pfeiffer F. (1995a): *Dynamic simulation of assembly processes.* — Proc. IEEE/RSJ Conf. *Int. Robots* and *Systems*, Pittsburgh, PA, Vol.2, pp.298–304.

Meitinger Th. and Pfeiffer F. (1995b): *Modeling and simulation of the assembly of snap joints.* — Proc. Int. Symp. *Assembly and Task Planning*, Pittsburgh, PA, pp.15–20.

Park Y.K. and Cho H.S. (1995): *A neural network-based assembly algorithm for chamferless parts mating.* — Proc. IEEE Symp. *Assembly and Task Planning*, Pittsburgh, PA, pp.381–386.

Park Y.K., Cho H.S. and Park J.O. (1992): *A fast searching method for precision parts mating based upon fuzzy logic approach.* — Proc. IEEE/RSJ Int. Conf. *Int. Robots and Systems*, Raleigh, NC, pp.1319–1323.

Pfeiffer F. and Glocker Ch. (1996): *Multibody Dynamics with Unilateral Contacts.* — New York: J. Wiley.

Pfeiffer F. (1990): *Dynamical Systems with Impact and Stick-Slip Phenomena.* — Toronto: CSME Mechanical Engineering Forum.

Seyfferth W. and Pfeiffer F. (1992): *Dynamics of assembly processes with a manipulator.* — Proc. IEEE/RSJ Int. Conf. Int. *Robots and Systems*, Raleigh, NC, pp.1303–1310.

Seyfferth W. (1993): *Modellierung unstetiger Montageprozesse mit Robotern.* — Fortschrittberichte VDI, Reihe 11, No.199, Düsseldorf (in German).

Steinle J. (1996): *Entwicklung einer prozeßangepaßten Roboterregelung für Montagevorgänge.* – Fortschrittberichte VDI, Reihe 8, No.548, Düsseldorf (in German).

Strip D. (1989): *A passive mechanism for insertion of convex pegs.* — Proc. IEEE Conf. *Robotics and Automation*, Scottsdale, AZ, pp.242–248.

Villarreal A. and Asada H. (1991): *A geometric representation of distributed compliance for the assembly of flexible parts.* — Proc. IEEE Conf. *Robotics and Automation*, Sacramento, CA, pp.2708–2715.

Wapenhans H., Seyfferth W. and Pfeiffer F. (1992): *Hybrid position and force control with unsteady assembly dynamics.* — Proc. IMACS/SICE Int. Symp. RMS^2, Kobe, Japan, pp.1279–1284.

Whitney D.E. (1982): *Quasi-static assembly of compliantly supported rigid parts.* — Trans. ASME J. Dyn. Syst., Meas. Contr., Vol.104, pp.65–77.

Whitney D.E., Gustavson R.E. and Hennessy M.P. (1983): *Designing chamfers.* — Int. J. Robot Res., Vol.2, No.4.

Wösle M. and Pfeiffer F. (1996): *Dynamics of multibody systems containing dependent unilateral constraints with friction.* — J. Vibration and Control, pp.161–192.

Xiao J. and Zhang L. (1995): *An efficient algorithm (FAPRIC) for finding the principal contacts possibly established due to uncertainties.* — Proc. IEEE Conf. *Robotics and Automation*, Nagoya, Japan, pp.427–432.